Microchimica Acta (2023) 190:153
https://doi.org/10.1007/s00604-023-05710-5

ORIGINAL PAPER

A novel fluorescent nanoprobe based on potassium permanganate–functionalized Ti_3C_2 QDs for the unique "turn-on" dual detection of Cr^{3+} and Hg^{2+} ions

Xiangjuan Zheng[1] · Zhiying Shi[1] · Chaojun Fu[1] · Yuanlin Ji[1] · Baozhu Chi[1] · Fanrong Ai[2] · Xiluan Yan[1,3]

Received: 24 November 2022 / Accepted: 19 February 2023 / Published online: 24 March 2023

Abstract

Titanium carbide quantum dots (Ti_3C_2 QDs) were synthesized by ammonia-assisted hydrothermal method. We also synthesized potassium permanganate ($KMnO_4$)–functionalized Ti_3C_2 QDs (Mn-QDs) by modifying Ti_3C_2 nanosheets with $KMnO_4$ and then cutting the functional nanosheets into Mn-QDs. The Ti_3C_2 QDs and Mn-QDs were characterized by fluorescence spectroscopy (FL), Fourier transform infrared spectroscopy (FTIR), UV–vis spectrophotometry (UV–vis), X-ray photoelectron spectroscopy (XPS), and transmission electron microscopy (TEM). Furthermore, the modified Mn-QDs have strong luminescence ability and good dispersion stability, which can be used for Cr^{3+} and Hg^{2+} double ion detection with enhanced fluorescence specificity. Cr^{3+}/Hg^{2+} and negatively charged Mn-QDs are bound together by electrostatic interactions. Meanwhile, the surface of Mn-QDs is rich in functional groups, which interacts with Cr^{3+}/Hg^{2+} to modify the surface traps, leading to defect passivation and exhibiting photoluminescence enhancement. For the dynamic quenching produced by the interaction of Mn-QDs with Hg^{2+} within 50 μM, it may be caused by the complex formation of Hg^{2+} trapped by the amino group on the surface of Mn-QDs. The detection limits for Cr^{3+} and Hg^{2+} were 0.80 μM and 0.16 μM, respectively. The recoveries of Cr^{3+} and Hg^{2+} ions in real water samples were 93.79–105.10% and 93.91–102.05%, respectively, by standard addition recovery test. In this work, the application of Mn-QDs in Cr^{3+} and Hg^{2+} ion detection was researched, which opens a new way for its application in the field of detecting heavy metal ions.

Keywords MXene · Quantum dots · Fluorescence · Heavy metal ions

Introduction

Nowadays, the environmental pollution caused by the discharge of industrial, agricultural, and household wastes has attracted people's attention. One of them is the water pollution caused by heavy metal ions. Among various heavy metal ions, chromium (III) ion (Cr^{3+}) plays a leading role in glucose metabolism and lipid metabolism, and is one of the essential trace elements for human body [1]. Deficiency of Cr^{3+} may lead to different health disorders, including disorders of lipid metabolism and diabetes. Likewise, high concentration levels of Cr^{3+} can also be harmful to our health and negatively affect cellular structure [2]. Another polluting heavy metal ion is mercury (II) ion (Hg^{2+}). Hg^{2+} readily penetrates the skin of respiratory and gastrointestinal tissues and causes irreversible damage to the central nervous system, leading to renal failure and various cognitive and motor impairments [3]. Meanwhile, the non-biodegradability and bioconcentration of Hg^{2+} in the environment bring about various serious diseases, including kidney diseases, skin diseases, and genotoxicity [4]. Even when present in trace amounts, it poses a serious biological threat. In consequence, it is necessary to explore an effective and rapid method to detect Cr^{3+} and Hg^{2+} in environmental samples. Until now, researchers have developed various methods for the detection of trace metal ions, such as atomic absorption\emission spectrometry [5], electrochemical techniques [6],

✉ Xiluan Yan
yanxiluan@ncu.edu.cn

1 School of Chemistry and Chemical Engineering, Nanchang University, Nanchang 330031, China

2 Bio 3D Printing Laboratory, School of Mechanical and Electrical Engineering, Nanchang University, Nanchang 330031, China

3 College of Pharmacy, Nanchang University, Nanchang 330031, China

and fluorescence spectrophotometry [1]. Among them, the fluorescence method has attracted much attention for its unique advantages such as simplicity, fast response, good selectivity, and high sensitivity.

MXene, whose chemical formula is $M_{n+1}X_n$, is a two-dimensional (2D) transition metal carbide or nitride, where *M* is the early transition metal, including Sc, Ti, and V, and *X* represents C and/or N. MXene is usually obtained by etching the $M_{n+1}AX_n$ phase (where *A* usually stands for elements III A or IV A), such as the typical material Ti_3AlC_2. Due to its abundant active sites, good biocompatibility, chemical stability, and surface hydrophilicity, MXene has attracted the attention of many researchers. It shows very good potential for applications in batteries, supercapacitors, photocatalytic applications, sensors, water treatment, and other fields [7–9]. The zero-dimensional (0D) MXene QDs derived from 2D MXene nanosheets (NSs) are able to inherit the advantages of MXene NSs in addition to showing unique optical and optoelectronic properties. It has promising applications in bioimaging, biosensing, antioxidant, antibacterial, ion detection, etc. [10–13]. Potassium permanganate ($KMnO_4$) is a common oxidant with a wide range of applications. After increasing the interlayer spacing by alkalinizing MXene NSs with potassium hydroxide (KOH), $KMnO_4$ was added and metal ions were further inserted into the interlayer to provide tunable properties. Furthermore, MXene can act as a reducing agent and undergo a redox reaction with $KMnO_4$, and the generated manganese dioxide (MnO_2) provides more active sites for the material [14, 15].

In the previous literatures, there are a lot of sensing materials for detecting metal ions. For example, Chen Lin et al. studied the organic framework of double layer interpenetrating double emission luminescent metal as Cr^{3+} ratio sensor [16]. Yi Zhang et al. synthesized CdS/CdS QDs as fluorescent sensors and liposome carriers for signal amplification to detect Hg^{2+} [17]. However, fluorescence sensors are often designed for one target detection, while those designed for simultaneous detection of two or more metal ions are rarely reported [18–21]. Besides, there are few reports on nanoprobes for the detection of Cr^{3+} and Hg^{2+} ions based on the MXene material field. Therefore, it is still a challenge to explore the relationship between MXene and multi-ion detection of heavy metals.

In this paper, Ti_3C_2 QDs (QDs) were firstly synthesized by ammonia-assisted hydrothermal method. Using ammonia ($NH_3{\cdot}H_2O$) as nitrogen source and $KMnO_4$ as functionalized reagent, $KMnO_4$-functionalized Ti_3C_2 QDs (Mn-QDs) were synthesized by hydrothermal shearing. The Mn-QDs exhibit bright blue-green under ultraviolet light and have an emission peak at 435 nm. Interestingly, compared with QDs without $KMnO_4$ treatment, Mn-QDs can specifically bind Cr^{3+} or Hg^{2+}. In the range of 0–2600 μM Cr^{3+}, Mn-QDs showed fluorescence enhancement by fluorescence measurement. After the addition of 0–550 μM Hg^{2+}, Mn-QD fluorescence decreased in the range of 0–50 μM and fluorescence increased in the range of 50 to 350 μM. As a result, we mainly explored a "turn-on" type nanoprobe for Mn-QDs that particularly detects double ions of Cr^{3+} and Hg^{2+}. To the best of our knowledge, this is the first attempt to functionalize QDs with $KMnO_4$ and apply them to the detection of bimetallic ions. This study opens up a new approach for the functional synthesis of Mn-QD nanomaterials and expands the application of MXene in ion monitoring of environmental pollution.

Experimental section

Chemical and apparatus

Related reagents and instruments have been included in the Electronic Supporting Information.

Preparation of Ti_3C_2 QDs (QDs)

The synthesis of QDs is an improvement on the previously reported process [22, 23]. Two grams of Ti_3AlC_2 powder was added to 40 mL 40% HF, stirred at 60 °C for 20 h, washed with pure water, centrifuged at 10,000 rpm for 10 min to collect precipitation, and vacuum dried at 60 °C for 24 h to obtain Ti_3C_2 MXene powder. Then, 0.25-g powder was placed in 17.5 mL deionized water and ultrasound was performed for 30 min, and 7.5 mL $NH_3{\cdot}H_2O$ was added subsequently. The mixture was transferred to a Teflon lined stainless steel autoclave and heated at 120 °C for 6 h. Finally, after the hydrothermal reaction has cooled to room temperature and centrifuged at 14,000 rpm for 30 min, the colorless and clear supernatant was retained and heated at 90 °C for 2 h to remove excess ammonia. QDs were obtained by 100-nm membrane filtration. The prepared colorless and clear solutions of QDs were stored at 4 °C for further characterization and application.

Synthesis of $KMnO_4$-functionalized Ti_3C_2 QDs (Mn-QDs)

The synthesis procedure of Mn-QDs is shown in Scheme 1. Briefly, the etched Ti_3C_2 MXene powder was added into 100 mL 3 mM KOH and stirred for 8 h. The turbid solution was centrifuged at 1000 rpm for 10 min, washed for several times, and dried, and the alkalized MXene powder was gained. The treated MXene powder was mixed with 10 mL 0.12 M $KMnO_4$ and 12 mM KCl solution, stirred for 30 min, then transferred to the reaction kettle, and heated at 140 °C for 8 h. The reaction was cooled before performing a series

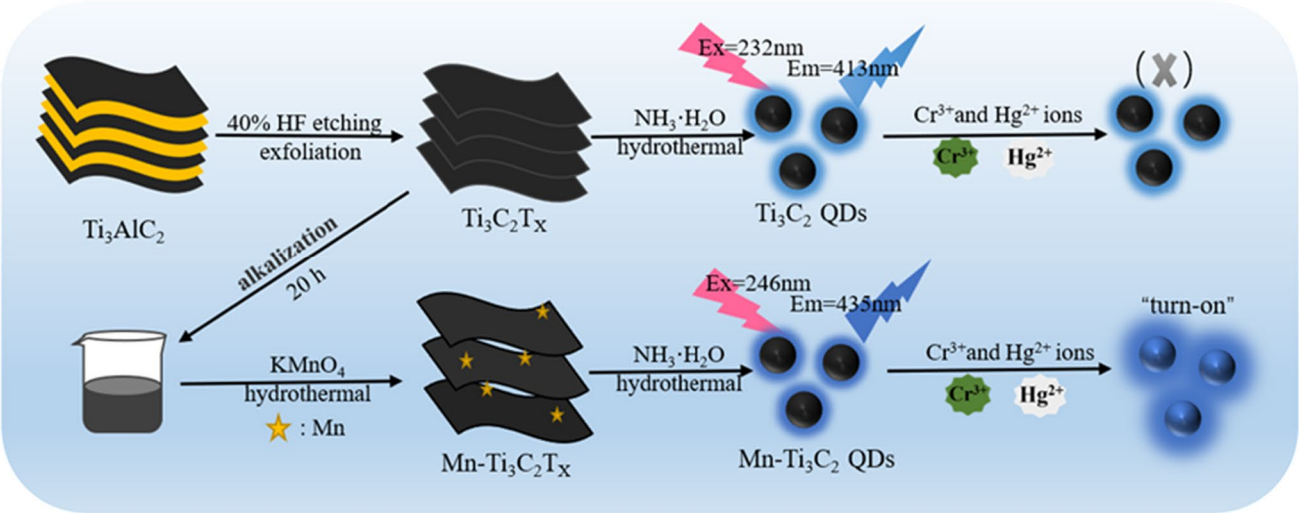

Scheme 1 Schematic representation for the preparation of Mn-QD nanoprobes and their applications for sensitive and selective fluorescence detection of Cr^{3+} and Hg^{2+} ions

of centrifugation and washing and drying procedures. And $KMnO_4$-functionalized MXene powder was gained. Afterwards, Mn-QDs can be obtained by the above QD synthesis operation. Similarly, the prepared material solution with light yellow was stored at 4 °C for later use. Mn-QD powder was obtained by freeze-drying for the further experimental characterization.

Determination of Cr^{3+} and Hg^{2+} ions

In this experiment, we took 10 µL Mn-QDs and added a certain concentration of Cr^{3+} or Hg^{2+}, mixing with pure water to a total volume of 400 mL. After reaction at room temperature for 10 min, FL measurements were recorded with 246-nm excitation. To test the selectivity of this material, other metal ions including Na^+, K^+, Al^{3+}, Mg^{2+}, Mn^{2+}, Co^{2+}, Ni^{2+}, Fe^{3+}, Fe^{2+}, Cu^{2+}, and Ag^+ were also examined by the same procedure. To determine whether the non-functionalized QDs interact with metal ions, the same series of ions (Na^+, K^+, Al^{3+}, Mg^{2+}, Mn^{2+}, Hg^{2+}, Co^{2+}, Cr^{3+}, Ni^{2+}, Fe^{3+}, Fe^{2+}, Cu^{2+}, and Ag^+) mixed with 100 µL QDs were also performed. The FL (λ_{ex} = 232 nm) of different ions were measured and compared with the above results. The emission and excitation slit widths of both QDs and Mn-QDs are 5 nm and 10 nm, and the measurement voltage is 700 V.

Fluorescence detection of nanoprobes in real samples

The practicality and feasibility of the Mn-QD nanoprobes for the detection of Cr^{3+} and Hg^{2+} in environmental samples were tested using two water samples, Runxi Lake and tap water, collected from the campus of Nanchang University. Prior to analysis, the water sample was treated by centrifugation to remove suspended particles. Then, Mn-QDs and known concentrations of Cr^{3+} and Hg^{2+} were added to the sample to determine the FL response of the solution. Calculate the recovery rate using the relationship in Formula 1:

$$\text{Recovery}(\%) = \frac{\text{Concentration of } Cr^{3+} \text{ or } Hg^{2+} \text{ found}}{\text{Concentration of } Cr^{3+} \text{or } Hg^{2+} \text{ added}} \times 100 \quad (1)$$

Results and discussion

Material characterization

On the one hand, the morphology, structure, and composition of the material were characterized in detail by TEM, XRD, XPS, and FTIR. The TEM images of the QDs and Mn-QDs are shown in Fig. 1. QDs and Mn-QDs exhibited nearly spherical particles with well monodispersity. The average lateral size of QDs was 1.64 ± 0.30 nm (n = 100), and the particle size distribution was mainly in the range of 1.2 to 2.4 nm. The average size of Mn-QDs was 2.24 ± 0.43 nm (n = 100), and the particle size distribution was mainly in the range of 1.6 to 3.2 nm. The crystallographic features of Mn-QD nanomaterials were further revealed by HRTEM images. Lattice fringes with spacing of 0.26 nm in the inner plane were measured (interpolation in Fig. 1E), corresponding to the (010) facet of Ti_3C_2 MXene [24, 25], which highlighted the crystalline nature of Mn-QDs.

The strongest peak (104) of Ti_3AlC_2 standard card is 39°, which is the characteristic peak of aluminum (Al) atom [26].

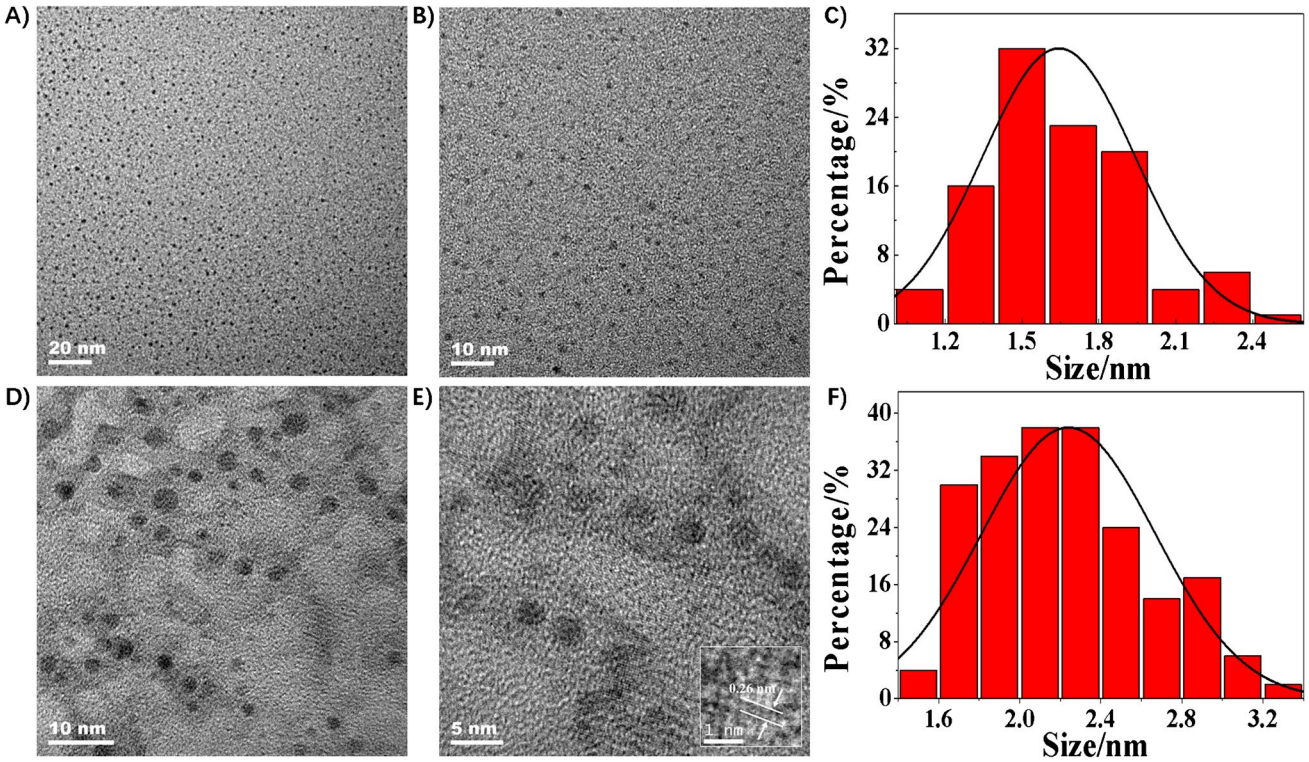

Fig. 1 TEM images of **A**, **B** QDs and **D** Mn-QDs. **E** HRTEM images of Mn-QDs with a lattice spacing of 0.26 nm. The size distribution of **C** QDs and **F** Mn-QDs

As shown in Fig. 2B, after HF etching, the 39° peak of QDs is significantly reduced or even disappears, indicating that the Al layer is successfully etched off. After the MXene hydrothermal reaction increased the layer spacing, the peaks of 41.7°, 28.6°, and 19° were enlarged and changed to the small angle direction of 40°, 28.1°, and 17.1° [27]. Furthermore, the two intense diffraction peaks located at 17.1° and 34.7°, which correspond to the (004) and (101) peaks of Ti_3C_2 MXene [28], respectively, indicate that QDs are successfully prepared and still maintain the 2D layered structure of MXene. On the basis of QDs, Mn-QDs exhibited the above phenomenon of weakening or disappearance of the strong peaks. After expanding the layer spacing of MXene by KOH alkalization treatment, the Mn-QDs derived from MXene were further modified with $KMnO_4$, and the insertion of foreign substances caused corresponding changes in the material structure [29–31]. The XRD images of the two do not match well, mainly due to the insertion of the exogenous material causes a corresponding change in the material structure. The peak appearing at 24° is TiO_2 formed by oxidation of MXene [32], indicating that QDs were successfully functionalized with $KMnO_4$.

FTIR was used to characterize the composition and chemical bond of the material, as shown in Fig. 2A, stretching vibration of hydroxyl (-OH) at 3420 cm^{-1} and 1401 cm^{-1}, vibration at 3113 cm^{-1} attributed to amino group (-NH), peak of 1627 cm^{-1} attributed to carbonyl group (C = O), and 1007 cm^{-1} band belongs to C-F bond [33–35]. In particular, the peaks at 705 cm^{-1} and 576 cm^{-1} are related to the vibrations of Ti–O and Ti-C bonds, respectively [36]. It is clear that the wavelengths of the functional groups of QDs and Mn-QDs fluctuate between 3500 and 2800 cm^{-1}. Due to the fact that the addition of $KMnO_4$ may have changed the surface structure of Mn-QDs, thus, changing the wavelengths and intensities of the functional groups also corroborates the change in the structure of their physical phases. The functional groups of QDs and Mn-QDs at 1600 to 600 cm^{-1} are matched one by one. Beyond that, the existence of bands 576 and 702 is also attributed to Mn–O vibration [37]. In summary, it can be indicated that Mn-QDs have been successfully prepared.

The chemical composition and overall structure of QDs and Mn-QDs were further investigated by XPS. The full-range XPS spectra of QDs showed five significant peaks at 285.2 (C 1 s), 401.8 (N 1 s), 532.2 (O 1 s), 684.9 (F 1 s), and 456.1 eV (Ti 2p), demonstrating the successful synthesis of QDs [12, 24]. The full-range XPS spectra of Mn-QDs showed five significant peaks at 285.0, 407.1, 532.1, 685.1, 455.3, 293.1, and 654.0 eV corresponding to C, N, O, F, Ti, K, and Mn elements [15, 38, 39], further indicating $KMnO_4$

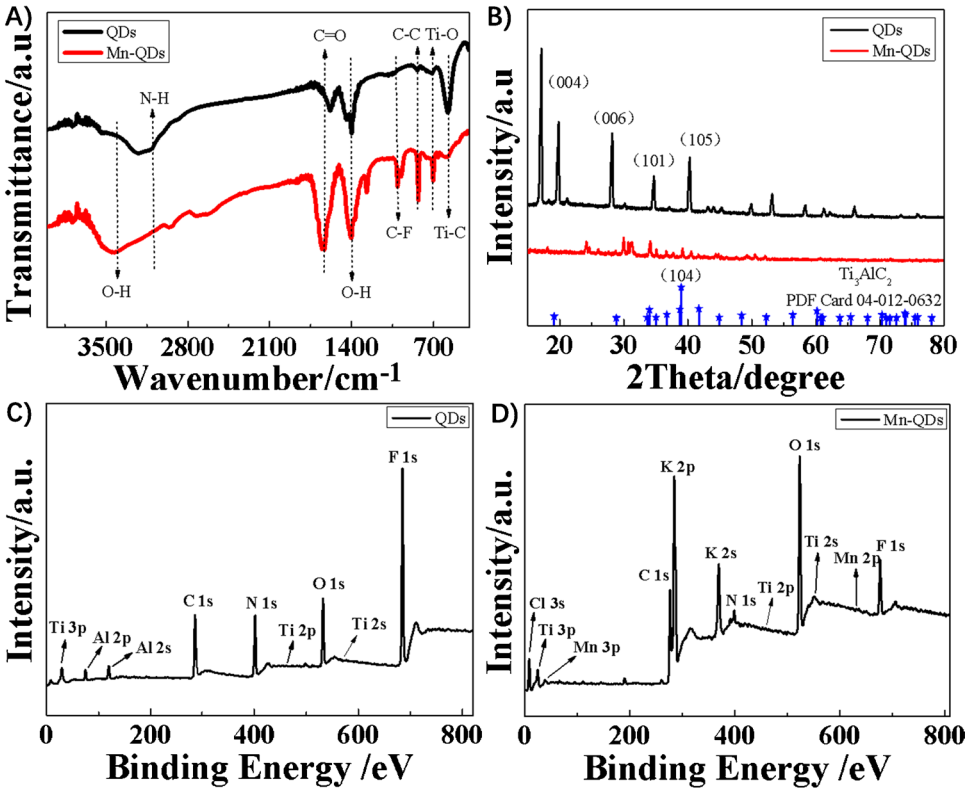

Fig. 2 **A** FTIR spectra of QDs and Mn-QDs. **B** XRD spectra of QDs and Mn-QDs. XPS spectra of **C** QDs and **D** Mn-QDs

successfully functionalized QDs. The enlarged characteristic spectra of C 1 s, O 1 s, K 2p, and Mn 2p are displayed in Fig. S1, respectively. And the detailed narrow spectrum analysis has been given in the supporting information. On the other hand, the optical properties of QDs and Mn-QDs were characterized. In Fig. 3A, the FL of QDs has two excitation peaks at about 232 nm and 321 nm and one emission peak (black line) at about 413 nm. The FL of Mn-QDs has two excitation peaks at about 246 nm and 314 nm and one emission peak at about 435 nm (red line). An obvious absorption peak located at 209 nm could be observed in the absorption spectrum of Mn-QDs (violet curve) when compared with that of QDs (blue curve), because of the trapping of the excited state energy by the surface states [40]. These changes of optical properties may be related to functionalization, and the embedding of external functional groups improves their optical properties. QDs are colorless and transparent under natural light (first from the left in the inset) and blue under 365-nm UV irradiation (first from the right), and Mn-QDs are a light yellow solution under natural light (second from the left) and blue-green under 365-nm UV light (second from the right). The excellent luminescence of Mn-QDs proves to be an ideal fluorescent probe material for ion detection. On the side, we performed an optimization test regarding the excitation wavelength of Mn-QDs, and as shown in Fig. 3B, the best display wavelength is 245 nm. In detail, the excitation wavelength of our subsequent experiments was concentrated at 246 nm.

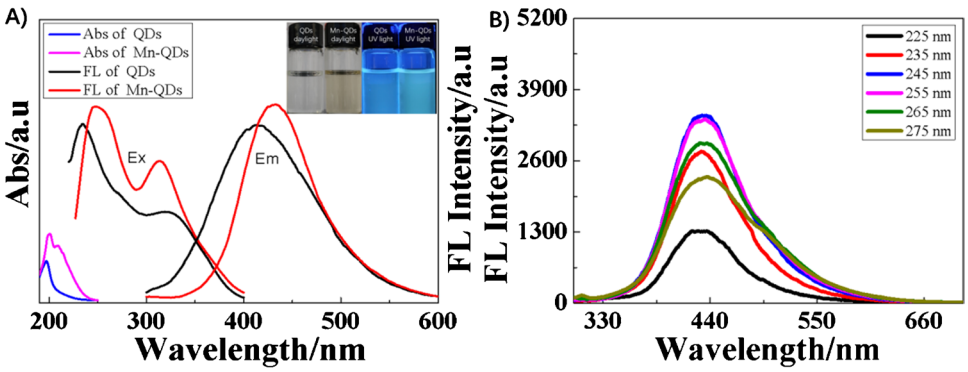

Fig. 3 **A** Absorption spectra of QDs (blue curve) and Mn-QDs (violet curve), fluorescence spectra of QDs (black curve) and Mn-QDs (red curve); insets show pictures of QDs and Mn-QDs under natural light and 365-nm UV light. **B** FL emission spectra recorded at diverse excitation wavelengths for Mn-QDs

Condition optimization and stability performance

To ensure the best FL performance, the synthesis conditions of Mn-QDs were firstly optimized. As shown in Fig. S2, the results showed that the best FL performance of Mn-QDs was achieved when the temperature was 120 °C, the time was 6 h, $KMnO_4$ doping amount was 10 mL, and ammonia/water ratio was 3/7. And then, in order to explore the practical application of Mn-QDs as nanoprobe in ion detection, it is necessary to examine the changes of their FL intensity under different concentrations of NaCl and pH environments. As shown in Fig. S3(A), the material can still maintain the same FL intensity at high and low salt concentrations. Figure S3(B) shows that the FL intensity of the material basically remained unchanged at pH 4–10, but decreased slightly when the pH exceeded 10. Figure S3(C) shows that the FL intensity of the material hardly changed after 55 days of storage, which indicates that the material is stable and can be stored for a long time. Finally, Mn-QDs also appeared outstanding optical stability. In Fig. S3(D), the FL intensity of Mn-QDs did not change significantly under 70-min continuous scanning ($\lambda_{ex} = 246$ nm). This indicates that Mn-QDs have good stability and are expected to be used in environmental applications.

In order to save the experimental cost, we optimized the usage of Mn-QDs. The solutions of 10, 20, 35, 50, and 65 µL Mn-QDs were taken separately and supplemented with pure water to 400 µL. FL was measured at 246-nm excitation. In Fig. S4, when the amount of Mn-QDs decreased, the emission peak of Mn-QDs appeared blue shift. This may be caused by the reduced content of Mn-QDs in the cuvette. Therefore, from the perspective of saving experimental costs, we selected 10 µL Mn-QDs for the subsequent ion experiments.

Determination of Cr^{3+} and Hg^{2+} ions by Mn-QDs

In this study, a novel fluorescence nanoprobe based on Mn-QDs was developed to respond to Cr^{3+} and Hg^{2+} ions simultaneously. We first evaluated the feasibility of the experiment. As shown in Fig. S5(A), when Mn-QDs were mixed with 500 µM Cr^{3+} or Hg^{2+}, the experimental phenomena of FL enhancement and peak blue shift of the mixed solution could be clearly observed, whereas the FL of the mixed solution did not change significantly when 500 µM Cr^{3+} or Hg^{2+} was added to QDs. Blank solutions of QDs and Mn-QDs were also measured and were able to exhibit lower FL intensities. Thus, the experiment was judged to be feasible. So as to explore possible practical applications, the effects of 13 common metal ions (Na^+, K^+, Al^{3+}, Mg^{2+}, Mn^{2+}, Co^{2+}, Hg^{2+}, Ni^+, Cr^{3+}, Fe^{3+}, Fe^{2+}, Cu^{2+}, and Ag^+ at 300 µM concentrations) on QDs and Mn-QD FL responses were studied. In Fig. S5(B), for Mn-QDs, FL enhancement efficiency of Cr^{3+} and Hg^{2+} ions calculated using the formula $(F - F_0)/F_0$ was found to reach 1.75 and 0.95, respectively. F_0 was the FL intensity of QDs or Mn-QDs, and F was the blank FL intensity of QDs or Mn-QDs reacting with metal ions. Figure S6 shows the fluorescence spectra of QDs and Mn-QDs in a series of different ions. As illustrated in Fig. 5B and Fig. S6, the addition of Cr^{3+} or Hg^{2+} has an obviously enhancing effect on the FL response of Mn-QDs; however, the others show minor influence on the response of Mn-QDs. Therefore, Mn-QDs have good selectivity for Cr^{3+} and Hg^{2+}.

Further analysis was performed for Cr^{3+} and Hg^{2+} ions. Figure 4A shows the FL response of Mn-QDs over the 0–2600 µM Cr^{3+} concentration range. The inset in Fig. 4A shows the photographs under daylight lamp and 365-nm UV lamp regarding the blank Mn-QD solution and the solution after the addition of 500 µM, 1500 µM, and 2600 µM Cr^{3+}. After the addition of Cr^{3+}, Mn-QDs reacted with them

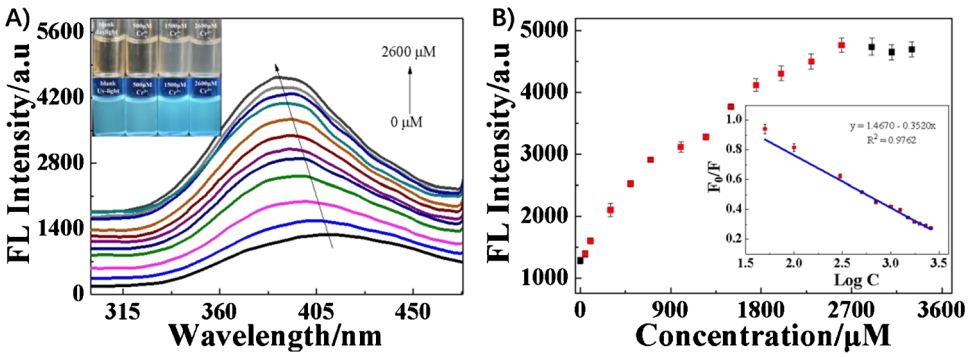

Fig. 4 **A** FL emission spectra of Mn-QDs in the presence of Cr^{3+} ion over 0–2600 µM. The inset shows photographs of Mn-QDs and the solution after the addition of Cr^{3+} under sunlight and UV lamps. **B** Plots of the FL versus Cr^{3+} concentration; the inset is the calibration curve of F_0/F and Cr^{3+} concentrations in the 50 to 2600 µM range. F_0 is the FL response of Mn-QDs; F is the FL response of Mn-QDs after the addition of Cr^{3+}. The error bars represent the standard deviation based on five independent measurements

resulting in the mixed solution gradually changing its color from light yellow to colorless. And the color of the solution changed from dark blue-green to bright blue under UV lamp. The FL intensity of Mn-QDs increased significantly with the increase of (0–2600 μM) Cr^{3+} concentration, while the blue-shift phenomenon occurred in the highest site peak. The linear range for Cr^{3+} is 50–2600 μM with a linear equation of $F_0/F = 1.4670 - 0.3520$ Log [Cr^{3+}] (μM) ($R^2 = 0.9762$, $n = 5$). The limits of detection (LOD) of the nanoprobe for Cr^{3+} was 0.80 μM, which was estimated from the formula of LOD = $3\sigma/K$ (σ shows the standard deviation of blank signal ($n = 5$) and K is the slope of the linear equation). The comparison of other methods for the detection of Cr^{3+} with this experiment is shown in Table 1. Compared with other materials, our work has a good LOD and a wider detection range. Besides, different from the FL enhancement method for Cr^{3+} detection in this paper, most other detection mechanisms are FL quenching.

The inset in Fig. 5A shows photographs about the blank Mn-QD solution and the solutions after the addition of 200 μM, 400 μM, and 600 μM Hg^{2+} under daylight lamp and 365-nm UV lamps. After adding Hg^{2+}, Mn-QDs reacted with them, resulting in the color of the mixed solutions gradually changing from yellow to light yellow. And the color of the solution changed accordingly under the UV lamp. Figure 5A shows that the FL response of Mn-QDs decreases with increasing Hg^{2+} concentration from 0 to 50 μM and increases from 50 to 550 μM Hg^{2+}. With the increase of Hg^{2+} concentration, the FL intensity of Mn-QDs decreases, while the peak undergoes a blue-shift phenomenon. When the Hg^{2+} concentration reached 65 μM, the FL intensity gradually showed an increasing trend. The top left inset in Fig. 5B shows the linear plot of the FL quenching of the Mn-QD solution after the addition of 0–50 μM Hg^{2+}. The linear equation for this interval is $F = 1212.58 - 5.5320$ [Hg^{2+}] (μM) ($R^2 = 0.9837$, $n = 5$). According to the illustration in the lower right corner, the linear range for Hg^{2+} is 50–550 μM and the linear equation is $F_0/F = 2.7399 - 0.8152$ Log [Hg^{2+}] (μM) ($R^2 = 0.9948$, $n = 5$). The LOD was 0.16 μM by calculating the 3 σ/K formula. The comparison of other methods for the detection of Hg^{2+} with this experiment is shown in Table 2. Compared to most of the fluorescence-off assays in the table, the FL "turn-on" type of this experiment has a wider detection range and good detection limits.

In this experiment, with the increase of the concentration of Cr^{3+} and Hg^{2+}, the maximum emission peak of Mn-QDs gradually shifted blue. Through zeta potential analysis, we can

Table 1 Comparison work of linear range and LOD for the detection of Cr^{3+} by FL assay using different materials

Materials (Cr^{3+})	Detection mechanism	Linear range (μM)	LOD (μM)	References
MoS_2 QDs	Fluorescence "turn-off"	0.1–100	0.08	[41]
NSCDs	Fluorescence "turn-off"	0–40	0.0078	[42]
DDCDs	Fluorescence "turn-off"	0.1–6.0	0.027	[43]
Zn-MOF	Fluorescence "turn-off"	50–300	5.55	[44]
S/NB-CQDs	Fluorescence "turn-off"	0–500	6	[45]
Rhodamine derivative	Fluorescence "turn-on"	0.5–20	0.17	[46]
Mn-QDs	Fluorescence "turn-on"	50–2600	0.80	This work

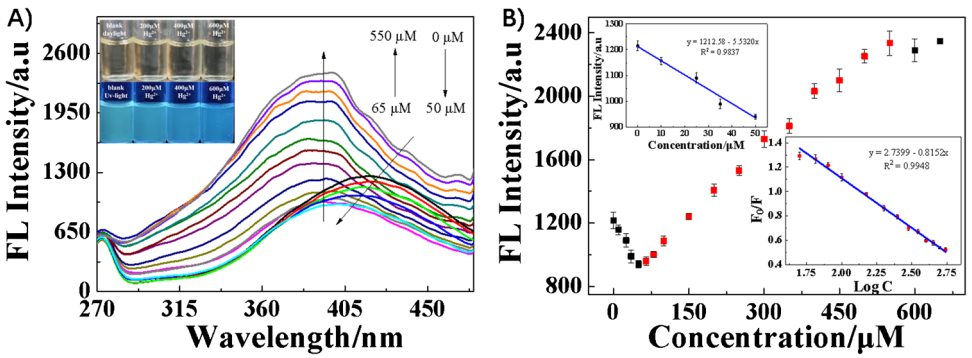

Fig. 5 **A** FL emission spectra of Mn-QDs in the presence of Hg^{2+} ion over 0–550 μM. The inset shows photographs of Mn-QDs and the solution after the addition of Hg^{2+} under sunlight and UV lamps. **B** Plots of the FL versus Hg^{2+} concentration. The inner illustration in the upper left corner is a linear FL quenching diagram of 0–50 μM Hg^{2+}. Another inset is linear relationship between F_0/F and Hg^{2+} concentrations in the range 50 to 550 μM. F_0 is the FL response of Mn-QDs and F is that of Mn-QDs with Hg^{2+}. The error bars are the same as those in Fig. 4

Table 2 Comparison work of linear range and LOD for the detection of Hg^{2+} by FL assay using different materials

Materials (Hg^{2+})	Detection mechanism	Linear range (μM)	LOD (μM)	References
ZnS: Ce QDs	Fluorescence "turn-off"	10–100	0.82	[47]
Exo III-assisted recycling Ti_3C_2	Fluorescence "turn-on"	0.00005–0.05	0.0000425	[48]
CdSe@ZnS QDs	Fluorescence "turn-off"	0–2	0.1	[49]
CdS: Eu QDs	Fluorescence "turn-off"	5–1000	2	[50]
CdSe/ZnS QDs	Fluorescence "turn-off"	0.1–100	0.09	[51]
Schiff base derivatives	Fluorescence "turn-on"	0.2–10	0.077	[52]
Mn-QDs	Fluorescence "turn-on"	50–550	0.16	This work

judge the binding between metal ions and Mn-QDs through electrostatic interaction, and the DLS data showed that average hydrodynamic radius of ultra-small Mn-QDs was also increased upon the addition of Cr^{3+} and Hg^{2+} ions (Supporting Information of Fig. S7A and S8). The strong interaction between Cr^{3+}/Hg^{2+} ion and Mn-QDs with abundant functional groups on the surface leads to the formation of ground state complex [53]. Furthermore, the average fluorescence decay time of Mn-QDs is 4.77 ns; however, it decreases to 3.57 and 1.71 ns by the addition of Cr^{3+} and Hg^{2+} ions (Supporting Information of Fig. S7D), which further confirms the formation of complexes between Mn-QDs and Cr^{3+}/Hg^{2+}.

When appropriate metal ions are added to the functionalized Mn-QDs, the D-orbital electrons of the existing metal ions can repel these trapped conduction band electrons, which is caused by the binding between the surface functional groups and the metal ions [54]. This association of metal ions promotes the complexation of electron–hole pairs, which restores the fluorescence intensity of the functionalized Mn-QDs. This is why the fluorescence intensity of each quantum dot increases with increasing metal ion concentration and shifts in wavelength.

Investigation into the response mechanism for Cr^{3+} and Hg^{2+}

To understand the fluorescence-on detection of Cr^{3+} and Hg^{2+} ions based on Mn-QD sensing nanoprobes, we performed a preliminary study of the response mechanism using zeta potential, fluorescence lifetime measurements, and absorption spectroscopy. As shown in Fig. S7(A), the zeta potential of Mn-QDs was − 47.9 mV. After mixing Mn-QDs with Cr^{3+} or Hg^{2+} solutions, the zeta potential increased to − 36.8 mV and − 13.65 mV, respectively. This indicates that there is an electrostatic interaction between Mn-QDs and Cr^{3+}/Hg^{2+} [55]. This also demonstrates that Mn-QDs and Cr^{3+}/Hg^{2+} can bind together. Furthermore, the small size and high quantum confinement effects of Mn-QDs lead to the formation of unsaturated bonds at their edges and surfaces, which exerted a higher chance to attach with other atoms [56].

The enhancement mechanism may be caused by passivation, absorption, and modification of the surface of Mn-QDs. The surface of Mn-QDs is rich in functional groups, which interact with Cr^{3+}/Hg^{2+} to modify the surface traps, resulting in passivation of defects and exhibiting photoluminescence enhancement [57, 58]. In addition, due to the similarity of Al atoms, the alkali metal ions (K element) may have the ability to inhibit the passivation defects generated during the preparation process, resulting in the FL enhancement of Mn-QDs [59].

To investigate the FL quenching mechanism of Mn-QDs and Hg^{2+}, the Stern–Volmer equation ($F_0/F = 1 + \mathrm{Ksv}\,[Q]$, where Ksv represents the quenching constant and $[Q]$ represents the concentration of the quenching agent) was used to determine the quenching mechanism [60]. As shown in Fig. S7 (B), a linear relationship between the F_0/F ratio and concentration of Hg^{2+} (10–50 μM) indicates that there is a dynamic quenching between Hg^{2+} and Mn-QDs. Meanwhile, the UV–vis of Mn-QDs showed some changes of absorption peaks after the addition of Hg^{2+}, which indicated that the FL quenching might be caused by the capture of Hg^{2+} by the amino groups on the surface of Mn-QDs to form Mn-QDs@Hg^{2+} complex [13, 61, 62]. The average fluorescence lifetime of QDs and Mn-QDs is 3.68 ns and 4.77 ns, respectively. Due to the fact that the functionalization of $KMnO_4$ may change the properties of the surface chemical states of QDs, the lifetime of Mn-QDs is prolonged [63]. After the addition of Hg^{2+}, the fluorescence lifetime of Mn-QDs decreased significantly to 1.71 ns. Besides, the value of τ_0/τ for static quenching (average fluorescence lifetime τ_0: QDs; τ: Mn-QDs@Hg^{2+}) should be 1, while $F_0/F = \tau_0/\tau$ should be valid for dynamic quenching [64]. It is calculated that $\tau_0/\tau = 4.77/1.71 = 2.79$. Therefore, the type of FL quenching of Mn-QDs induced by Hg^{2+} was dynamic quenching, which was consistent with the conclusion obtained from the study of the Stern–Volmer equation.

Fluorescence detection of Cr^{3+}/Hg^{2+} ions in real samples

The practicality and reliability of the Mn-QDs probe in detecting environmental samples were tested using samples

from Runxi Lake and tap water of Nanchang University. In the present experiments, the Cr^{3+}/Hg^{2+} solution with different concentrations was dropped into the pretreated real samples by standard addition method and then analyzed via the proposed approach. The specific procedure is that when a certain concentration of Cr^{3+} or Hg^{2+} ions was added to the Runxi Lake and tap water samples, their signals are measured by fluorescence spectrometry. Their recovery values can then be calculated by the corresponding linear equations. The measured results are summarized in Table S1 and Table S2. It can be clearly seen that the recoveries of Cr^{3+} and Hg^{2+} in water samples were 93.79–105.10% and 93.91–102.05%, respectively, with the relative standard deviations (RSD) of 0.86–3.32% and 0.66–5.00%. The results indicate that the method has great potential for the analysis of Cr^{3+} and Hg^{2+} ions in real samples.

Conclusion

In summary, Mn-QDs were prepared from $KMnO_4$-functionalized MXene NSs by a hydrothermal reaction. The Mn-QDs displayed well-monodispersed near-spherical particles with average size of 2.24 nm and exhibited brightly blue-green emission and good long-term storage stability. In addition, Mn-QDs were used as a simple and reliable turn-on fluorescent nanoprobe for the sensitive and simultaneous detection of Cr^{3+} and Hg^{2+} ions. The surface trap of Mn-QDs was modified by binding Cr^{3+}/Hg^{2+} through electrostatic interaction, which led to the passivation of surface defects and enhanced photoluminescence. This work not only leads to the development of a sensitive fluorescence assay for the detection of heavy metal ions, but also opens up a new and exciting channel for functionalized applications of MXene.

Supplementary Information The online version contains supplementary material available at https://doi.org/10.1007/s00604-023-05710-5.

Funding This work was financially supported by the Natural Science Foundation of Jiangxi Province (20212BAB206093) and the National Natural Science Foundation of China (nos. 22064012, 21907048, 31960207, and 81860610).

Declarations

Conflict of interest The authors declare no competing interests.

References

1. Dey G, Venkateswarulu M, Vivekananthan V et al (2016) Subpicomolar recognition of Cr^{3+} through bioinspired organic–inorganic ensemble utilization. ACS sensors 1(6):663–669
2. Saha S, Mahato P, Reddy GU et al (2012) Recognition of Hg^{2+} and Cr^{3+} in physiological conditions by a rhodamine derivative and its application as a reagent for cell-imaging studies. Inorg Chem 51(1):336–345
3. Hu PP, Liu N, Wu KY et al (2018) Successive and specific detection of Hg^{2+} and I^- by a DNA@MOF biosensor: experimental and simulation studies. Inorg Chem 57(14):8382–8389
4. Pang X, Bai H, Zhao H et al (2021) Biothiol-functionalized cuprous oxide sensor for dual-mode sensitive Hg^{2+} detection. ACS Appl Mater Interfaces 13(39):46980–46989
5. Borowska M, Jankowski K (2020) Sensitive determination of bioaccessible mercury in complex matrix samples by combined photochemical vapor generation and solid phase microextraction coupled with microwave induced plasma optical emission spectrometry. Talanta 219:121162
6. Yu J, Zhang X, Zhao M et al (2021) Fabrication of the Ni-based composite wires for electrochemical detection of copper(II) ions. Anal Chim Acta 1143:45–52
7. Qin R, Shan G, Hu M et al (2021) Two-dimensional transition metal carbides and/or nitrides (MXenes) and their applications in sensors. Materials Today Physics 21:100527
8. Meng W, Liu X, Song H et al (2021) Advances and challenges in 2D MXenes: from structures to energy storage and conversions. Nano Today 40:101273
9. Yu L, Chang J, Zhuang X et al (2022) Two-dimensional cobalt-doped Ti_3C_2 MXene nanozyme-mediated homogeneous electrochemical strategy for pesticides assay based on in situ generation of electroactive substances. Anal Chem 94(8):3669–3676
10. Lu S, Sui L, Liu Y et al (2019) White photoluminescent Ti_3C_2 MXene quantum dots with two-photon fluorescence. Adv Sci (Weinh) 6(9):1801470
11. Xue Q, Zhang H, Zhu M, et al (2017) Photoluminescent Ti_3C_2 MXene quantum dots for multicolor cellular imaging. Adv Mater Weinheim 29:15
12. Wang L, Zhang N, Li Y et al (2021) Mechanism of nitrogen-doped Ti_3C_2 quantum dots for free-radical scavenging and the ultrasensitive H_2O_2 detection performance. ACS Appl Mater Interfaces 13(36):42442–42450
13. Luo W, Liu H, Liu X et al (2021) Biocompatibility nanoprobe of MXene N-Ti_3C_2 quantum dot/Fe^{3+} for detection and fluorescence imaging of glutathione in living cells. Colloids Surf, B 201:111631
14. Pandey RP, Rasool K, Madhavan VE et al (2018) Ultrahigh-flux and fouling-resistant membranes based on layered silver MXene $Ti_3C_2T_x$ nanosheets. J Mater Chem A Mater Energy Sustain 6(8):3522–3533
15. Zhu X, Cao Z, Wang W et al (2021) Superior-performance aqueous zinc-ion batteries based on the in situ growth of MnO_2 nanosheets on V_2CT_X MXene. ACS Nano 15(2):2971–2983
16. Lin C, Wang M, Tang J et al (2021) A two-fold interpenetrated dual-emitting luminescent metal-organic framework as a ratiometric sensor for chromium(III). Inorg Chem 60(21):16803–16809
17. Zhang Y, Xiao JY, Zhu Y et al (2020) Fluorescence sensor based on biosynthetic CdSe/CdS quantum dots and liposome carrier signal amplification for MERCURY DEtection. Anal Chem 92(5):3990–3997
18. Kaur N, Kaur P, Singh K (2016) Ferrocene-BODIPY Push–Pull dyad: a common platform for the sensing of Hg^{2+} and Cr^{3+}. Sensors Actuators B Chem 229:499–505
19. Yang Y, Feng Y, Wang Y et al (2017) A novel ratiometric fluorescent probe for selective detection of Hg^{2+}, Cr^{3+} and Al^{3+} and its bioimaging application in living cells. Sens Actuators, B Chem 253:1055–1062
20. Mahato P, Saha S, Suresh E et al (2012) Ratiometric detection of Cr^{3+} and Hg^{2+} by a naphthalimide-rhodamine based fluorescent probe. Inorg Chem 51(3):1769–1777
21. Zhan L, Yang T, Zhen S J, et al (2017) Cytosine triphosphate-capped silver nanoparticles as a platform for visual and

colorimetric determination of mercury(II) and chromium(III). Mikrochimica Acta 184(9)3171–3178
22. Ai F, Fu C, Cheng G et al (2021) Amino-functionalized Ti_3C_2 MXene quantum dots as photoluminescent sensors for diagnosing histidine in human serum. ACS applied nano materials 4(8):8192–8199
23. Fu C, Ai F, Huang J et al (2022) Eu doped Ti_3C_2 quantum dots to form a ratiometric fluorescence platform for visual and quantitative point-of-care testing of tetracycline derivatives. Spectrochim Acta A Mol Biomol Spectrosc 272
24. X Zhou Q, Wang J, Li B, et al (2020) Dual emission reverse change ratio photoluminescence sensor based on a probe of nitrogen doped Ti_3C_2 quantum dots@DAP to detect H_2O_2 and xanthine. Anal Chem 92(11):7770. Washington
25. Zeng Z, Yan Y, Chen J, et al (2019) Boosting the photocatalytic ability of Cu_2O nanowires for CO_2 conversion by MXene quantum dots. Adv Funct Mater 29:2
26. Li Y, Ding L, Guo Y et al (2019) Boosting the photocatalytic ability of g-C_3N_4 for hydrogen production by Ti_3C_2 MXene quantum dots. ACS Appl Mater Interfaces 11(44):41440–41447
27. Lai C, An Z, Yi H et al (2021) Enhanced visible-light-driven photocatalytic activity of bismuth oxide via the decoration of titanium carbide quantum dots. J Colloid Interface Sci 600:161–173
28. Yang Y, Zeng Z, Zeng G et al (2019) Ti_3C_2 Mxene/porous g-C_3N_4 interfacial Schottky junction for boosting spatial charge separation in photocatalytic H_2O_2 production. Appl Catal B 258:117956
29. Lukatskaya MR, Mashtalir O, Ren CE et al (2013) Cation intercalation and high volumetric capacitance of two-dimensional titanium carbide. Science 341(6153):1502–1505
30. Wang C, Xie H, Chen S et al (2018) Atomic cobalt covalently engineered interlayers for superior lithium-ion storage. Adv Mater 30(32):e1802525
31. Wu J, Yang Q, Li Q et al (2021) Two-dimensional MnO_2 nanozyme-mediated homogeneous electrochemical detection of organophosphate pesticides without the interference of H_2O_2 and color. Anal Chem 93(8):4084–4091
32. Li Y, Xu D, Zhang D et al (2019) Study on MnO_2/MXene–Ti_3C_2 composite materials as cathode materials for magnesium batteries. RSC Adv 9(58):33572–33577
33. Guan Q, Ma J, Yang W et al (2019) Highly fluorescent Ti_3C_2 MXene quantum dots for macrophage labeling and Cu^{2+} ion sensing. Nanoscale 11(30):14123–14133
34. Yang F, Ge Y, Yin T et al (2020) $Ti_3C_2T_x$ MXene quantum dots with enhanced stability for Ultrafast Photonics. ACS applied nano materials 3(12):11850–11860
35. Yang EJ, Jeon OS, Yang JU et al (2020) Room temperature manufacturing photoluminescent graphene quantum dots based on MXene. Carbon (New York) 167:863–869
36. Liu M, He Y, Zhou J et al (2020) A "naked-eye" colorimetric and ratiometric fluorescence probe for uric acid based on Ti_3C_2 MXene quantum dots. Anal Chim Acta 1103:134–142
37. Aadil M, Mahmood M, Warsi MF et al (2021) Fabrication of MnO_2 nanowires and their nanohybrid with flat conductive matrix for the treatment of industrial effluents. FlatChem 30:100316
38. Huang D, Wu Y, Ai F, et al (2021) Fluorescent nitrogen-doped Ti_3C_2 MXene quantum dots as a unique on off on nanoprobe for chrominum VI and ascorbic acid based on inner filter effect. Sensors Actuators B Chem 342:130074
39. Gao M, Song Y, Liu Y et al (2021) Controlled fabrication of Au@MnO_2 core/shell assembled nanosheets by localized surface plasmon resonance. Appl Surf Sci 537:147912
40. Jiang X, Wang H, Shen Y, et al (2022) Nitrogen-doped Ti_3C_2 MXene quantum dots as novel high-efficiency electrochemiluminescent emitters for sensitive mucin 1 detection. Sensors Actuators B Chem 350:130891
41. Desai ML, Jha S, Basu H et al (2020) Simple hydrothermal approach for synthesis of fluorescent molybdenum disulfide quantum dots: sensing of Cr^{3+} ion and cellular imaging. Mater Sci Eng C Mater Biol Appl 111:110778
42. Guo J, Ye S, Li H et al (2021) Novel fluorescent probes based on nitrogen-sulfur Co-doped carbon dots for chromium ion detection. New J Chem 45(1):4828–4834
43. Lu H, Xu S, Liu J (2019) One pot generation of blue and red carbon dots in one binary solvent system for dual channel detection of Cr^{3+} and Pb^{2+} based on ion imprinted fluorescence polymers. ACS Sens 4(7):1917–1924
44. Jin H, Xu J, Zhang L et al (2018) Multi-responsive luminescent sensor based on Zn (II) metal-organic framework for selective sensing of Cr(III), Cr(VI) ions and p-nitrotolune. J Solid State Chem 268:168–174
45. Wang C, Xu J, Li H et al (2020) Tunable multicolour S/N Co-doped carbon quantum dots synthesized from waste foam and application to detection of Cr^{3+} ions. Luminescence (Chichester, England) 35(8):1373–1383
46. Li D, Li C, Qi H et al (2016) Rhodamine-based chemosensor for fluorescence determination of trivalent chromium ion in living cells. Sens Actuators, B Chem 223:705–712
47. Chu H, Yao D, Chen J et al (2020) Double-emission ratiometric fluorescent sensors composed of rare-earth-doped ZnS quantum dots for Hg^{2+} detection. ACS Omega 5(16):9558–9565
48. Lu L, Han X, Lin J et al (2021) Ultrasensitive fluorometric biosensor based on Ti_3C_2 MXenes with Hg^{2+}-triggered exonuclease III-assisted recycling amplification. Analyst 146(8):2664–2669
49. Cao B, Yuan C, Liu B et al (2013) Ratiometric fluorescence detection of mercuric ion based on the nanohybrid of fluorescence carbon dots and quantum dots. Anal Chim Acta 786:146–152
50. Zhang KX, Yu YX, Sun SQ (2013) Facile synthesis L-cysteine capped CdS: Eu quantum dots and their H^{g2}+ sensitive properties. Appl Surf Sci 276:333–339
51. Li H, Wang W, Wang Z et al (2021) Analyte-enhanced photocatalytic activity of CdSe/ZnS quantum dots for paper-based colorimetric sensing of Hg^{2+} under visible light. Microchem J 164:106037
52. Wen X, Fan Z (2017) A novel 'turn-on' fluorescence probe with aggregation-induced emission for the selective detection and bioimaging of Hg^{2+} in live cells. Sens Actuators, B Chem 247:655–663
53. Desai ML, Basu H, Singhal RK et al (2019) Ultra-small two dimensional MXene nanosheets for selective and sensitive fluorescence detection of Ag^+ and Mn^{2+} ions. Colloids Surf, A 565:70–77
54. Lin T, Dhenadhayalan N, Lee H et al (2019) Fluorescence turn-on chemosensors based on surface-functionalized MoS_2 quantum dots. Sens Actuators, B Chem 281:659–669
55. Chen X, Sun X, Xu W et al (2018) Ratiometric photoluminescence sensing based on Ti_3C_2 MXene quantum dots as an intracellular pH sensor. Nanoscale 10(3):1111–1118
56. Wang H, Zhao R, Hu H et al (2020) 0D/2D Heterojunctions of Ti_3C_2 MXene QDs/SiC as an efficient and robust photocatalyst for boosting the visible photocatalytic NO pollutant removal ability. ACS Appl Mater Interfaces 12(36):40176–40185
57. Wang H, Zhu W, Fang M et al (2016) Turn-on fluorescence probe for high sensitive and selective detection of Ag^+ by L-glutathione capped CdTe quantum dots in aqueous medium. J Lumin 180:14–19
58. Ge J, Li W, He X et al (2020) Charge behavior modulation by titanium-carbide quantum dots and nanosheets for efficient perovskite solar cells. Materials today energy 18:100562
59. Zhang S, Qi Z, Li Y (2022) Alkali preparation and ions detection of Ti_3C_2 quantum dots. Ceram Int 48(15):21118–21124

60. Zhong Y, Yi T (2019) MoS_2 quantum dots as a unique fluorescent "turn-off-on" probe for the simple and rapid determination of adenosine triphosphate. Journal Of Materials Chemistry B 7(15):2549–2556
61. Feng Y, Zhou F, Deng Q et al (2020) Solvothermal synthesis of in situ nitrogen-doped Ti_3C_2 MXene fluorescent quantum dots for selective Cu^{2+} detection. Ceram Int 46(6):8320–8327
62. Wan M, Zhou J, Yang H, et al (2022) Covalently N-doped MXene quantum dots for highly stable fluorescent Cu^{2+} ion sensor. ACS Appl Nano Mater
63. Xu Q, Ding L, Wen Y, et al (2018) High photoluminescence quantum yield of 18.7% by using nitrogen- doped Ti_3C_2 MXene quantum dots. J Mater Chem C 6(24)6360–6369
64. Behera PK, Mukherjee T, Mishra AK (1995) Simultaneous presence of static and dynamic component in the fluorescence quenching for substituted naphthalene—CCl_4 system. J Lumin 65(3):131–136